

Article

An Impeller Optimization Method for the High Specific Speed Mixed-Flow Reactor Coolant Pump Applied to Marine Nuclear Power

Qiang Fu ¹, Yun Zhao ¹, Yonggang Lu ^{2,3,*} , Weiqiang Zhao ³  and Rongsheng Zhu ¹ 

¹ National Research Center of Pumps, Jiangsu University, Zhenjiang 212013, China; ujsfq@sina.com (Q.F.); 2222211036@stmail.ujs.edu.cn (Y.Z.); ujs_zrs@163.com (R.Z.)

² School of Energy and Power Engineering, Jiangsu University, Zhenjiang 212013, China

³ Department of Energy and Power Engineering, Tsinghua University, Beijing 100084, China; zhaoweiqiang@mail.tsinghua.edu.cn

* Correspondence: luyg@mail.tsinghua.edu.cn

Abstract: The reactor coolant pump (RCP) is the only rotating equipment in the primary circuit system of a nuclear power plant and the “heart” of the nuclear reactor. The L formula is defined, and the L/h_{imp} is introduced to study the influence of impeller blade type on the performance of the RCP. Twenty groups of models are designed, the concept of arc height ratio is proposed from the perspective of h_{imp} and L , and the distribution of internal entropy production within the impeller of the RCP under different L s and h_{imps} of the impeller blade type is analyzed. The results show that when h_{imp} remains un-changed and L increases, the low-pressure area at the inlet of the impeller expands while the high-pressure area at the outlet decreases under the design flow or large flow conditions. The smoother blade profile reduces the occurrence of secondary flow phenomena and makes the RCP pressure distribution more uniform. Under design flow and large flow conditions, smaller L/h_{imp} and higher h_{imp} lead to higher efficiency and head performance. However, higher efficiency and lower head performance can be achieved under small flow conditions with larger L/h_{imp} and lower h_{imp} .

Keywords: mixed-flow reactor coolant pump; arc high ratio; optimization; entropy production theory; hydraulic loss



Citation: Fu, Q.; Zhao, Y.; Lu, Y.; Zhao, W.; Zhu, R. An Impeller Optimization Method for the High Specific Speed Mixed-Flow Reactor Coolant Pump Applied to Marine Nuclear Power. *J. Mar. Sci. Eng.* **2023**, *11*, 1301. <https://doi.org/10.3390/jmse11071301>

Academic Editor: Unai Fernandez-Gamiz

Received: 20 May 2023
Revised: 23 June 2023
Accepted: 23 June 2023
Published: 26 June 2023



Copyright: © 2023 by the authors. Licensee MDPI, Basel, Switzerland. This article is an open access article distributed under the terms and conditions of the Creative Commons Attribution (CC BY) license (<https://creativecommons.org/licenses/by/4.0/>).

1. Introduction

The Pressurized Water Reactor (PWR) is the most technologically mature marine nuclear reactor at present, which can be applied to floating power stations, nuclear submarines, nuclear-powered icebreakers, and marine resources development. It is an important measure to solve future offshore energy problems. The Reactor Coolant Pump (RCP) is the “heart” of a nuclear reactor and the only rotating equipment in the primary circuit system of a nuclear power plant [1]. Its primary function is to ensure the circulation of the nuclear primary coolant and remove heat from the core during regular operation. As the primary energy-consuming equipment in nuclear power plants, the RCP’s continuous and stable operation has a critical impact on the safety and stability of the entire plant [2]. Therefore, developing an efficient hydraulic model for the RCP is essential.

In recent years, scholars have conducted extensive analysis of the high-efficiency hydraulic model and internal flow field of pumps. The study of impellers mainly focuses on the in-depth exploration of geometric parameters such as blade thickness distribution, pack angle, and blade inlet position, and finding the optimal values of these parameters using genetic algorithms. Yang Minguan et al. [3] discovered that an impeller with a maximum thickness of about 1/3 of the blade area from the inlet can achieve relatively high hydraulic efficiency, and that an impeller with a rounded blade working face has

the best hydraulic performance [4]. Qiu W et al. [5] found that within a certain range, the larger the impeller pack angle, the better the inertia performance of the corresponding pump; the smaller the number of impeller blades, the better the inertia performance of the corresponding pump. Sambhrant et al. [6] found that at the impeller entrance, the inclined blade position was more suitable than the trapezoidal blade, because the paradigm iso effect force distribution is smaller in the inlet inclined blade. Wang Xiuli et al. [7] discovered that the dominant frequency of the impeller remains unchanged with changes in flow or inlet diameter of the short blade. The high frequency of the suction side of the blade gradually decreases, while the high frequency of the pressure face gradually increases with an increase in the inlet diameter of the short blade. Al-Obaidi [8] found that the number of impeller blades has a high impact on pressure, shear stress, magnitude velocity, axial velocity, radial velocity, tangential velocity, and average pressure, and he also [9] studied the behaviors of the flow field and pressure fluctuations in both time and frequency domains in an axial flow pump via the changing of various impeller blade angles. Li H [10] found that different impeller trailing edges can affect the efficiency of the pump; the thinner the trailing edge, the higher the efficiency. Wang H [11] variously tested slot structure geometric parameter combinations to explore this relationship: slot position p , slot width b_1 , slot deflection angle β , and slot depth h with (3–4) levels were selected for each factor on an L_{16} orthogonal test table, and the results show that b_1 and h are the major factors influencing pump performance under small and rated flow conditions. Xie Rong et al. [12] utilized an optimized Latin hypercube experimental design method to analyze the impact of impeller geometry and its distance from the guide vane inlet on the hydraulic performance of an RCP. Lu Yeming [13,14] employed a united optimal design technology to evaluate the effects of crucial structures (impeller and vane blades) on pump performance. They determined that swirl velocity and installation angle were key design variables for the impeller blades and vane blades, respectively. D X Ye [15] proposed an optimization approach based on the Kriging model and genetic algorithm, utilizing an experimental design with a Latin Hypercube to create 16 design cases containing three main parameters of blade: inlet angle β_1 , pack angle ϕ , and outlet blade angle β_2 .

Most previous studies have focused on analyzing individual parameters of the impeller or using algorithms to analyze the optimal values of a few parameters but have yet to consider the coupling relationships between parameters to analyze the influence of impeller geometry on hydraulic performance. This study focuses on a mixed-flow RCP with $ns = 461$, which utilizes the design concept of axial flow pumps for impeller blade-type design. The L formula is defined, and the L/h_{imp} is introduced to study the influence of impeller blade type on the performance of the RCP. Twenty groups of models are designed according to the orthogonal test method, the concept of arc height ratio is proposed from the perspective of h_{imp} and L , and the distribution of internal entropy production within the impeller of the RCP under different L s and h_{imp} s of the impeller blade type is analyzed. By studying the flow loss of the RCP, the study derives the effect of h_{imp} and L on the hydraulic performance of the RCP.

2. Materials and Methods

This study focuses on the mode pump of a mixed-flow RCP with a scaling ratio of 2.866 and a specific speed of 461. The fluid medium density in the pump is 997.561 kg/m^3 , and the dynamic viscosity of the fluid medium is $8.8871 \times 10^{-4} \text{ Pa}\cdot\text{s}$. Table 1 illustrates the scaled model pump parameters. The impeller and guide vane are built using CFTurbo software, while a class of spherical snail casing is built using three-dimensional software CREO. Figure 1 depicts the fluid calculation domain of the RCP.

Table 1. Main parameters of the RCP.

Parameter	Value	Parameter	Value
Rated flow, Q_d	1080 m ³ /h	Impeller inlet diameter, D_1	230 mm
Rated head, H_d	12 m	Impeller outlet diameter, D_2	278 mm
Rated speed, n	1485 r/min	Number of impeller blades, Z_i	4
Impeller outlet width, b_2	99 mm	Number of guide vane blades, Z_d	11

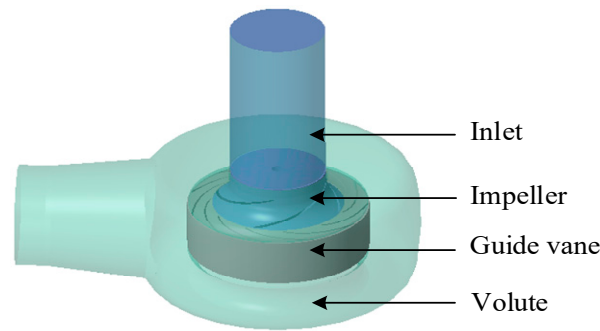


Figure 1. Fluid domain of the RCP.

Mixed flow pumps have a specific speed ranging from 300 to 500, while axial flow pumps range from 500 to 1200. The specific speed of the RCP examined in this study is 461, which can be either an axial or mixed flow solution at this parameter. Axial flow pumps operate based mainly on the basic theory of lift forces in fluid mechanics. When the centrifugal impeller runs at high speed, the fluid in the casing is primarily subject to the radial lift force of the impeller to perform work. The design method of traditional mixed flow pumps is basically the same as that of centrifugal pumps. It does not take into account the influence of the radial lift forces on the fluid in the impeller, while the fluid in the impeller of mixed flow pumps is subject to both centrifugal and radial lift forces.

The geometry parameters of axial flow pump impellers mainly consist of chord length, outlet diameter, pitch, blade overlap coefficient, inlet and outlet angles, and hub ratio. This study incorporates the design philosophy of axial flow pumps and axial flow impeller design by treating the blades as made up of infinite arcs. The vanes are unfolded to examine the impact of impeller blades on the hydraulic performance of RCP concerning arc length (chord length and blade overlap coefficient), blade height (outlet diameter and hub ratio), and the interaction between them.

The K_1 factor is used to represent the arc length on the horizontal plane, while the K_2 coefficient is introduced to correct errors resulting from the angle of repose and to make the arc length on the horizontal plane more accurate. The K_2 coefficient accomplishes this by adding an import/export width difference parameter, thereby converting a planar arc length into a spatial arc length, as illustrated in Figure 2. The arc length is calculated using the following formula:

$$L = \frac{1}{2}(L_H + L_S) = \sqrt{\left[\frac{[K_1 D_1 + (1 - K_1) D_2] \times \phi}{\cos[K_2 \beta_1 + (1 - K_2) \beta_2]} \right]^2 + \left[\frac{1}{2}(b_1 - b_2) \right]^2}, \quad (1)$$

$$h_{imp} \approx \frac{1}{2}(h_L + h_T) = \frac{1}{2}(b_1 + b_2), \quad (2)$$

where ϕ is the pack angle of the impeller blade; K_1 and K_2 are the correction factors; K_1 is 1.9274, K_2 is 0.5246; D_1, D_2 are the inlet and outlet diameters of the impeller; β_1, β_2 are the inlet and outlet placement angles of the impeller; b_1 and b_2 are the inlet and outlet widths of impeller; L_H is the hub length; L_S is the shroud length; h_{imp} is the blade height; h_L is the leading edge length; h_T is the trailing edge length; and L/h_{imp} is the ratio of arc length to blade height.

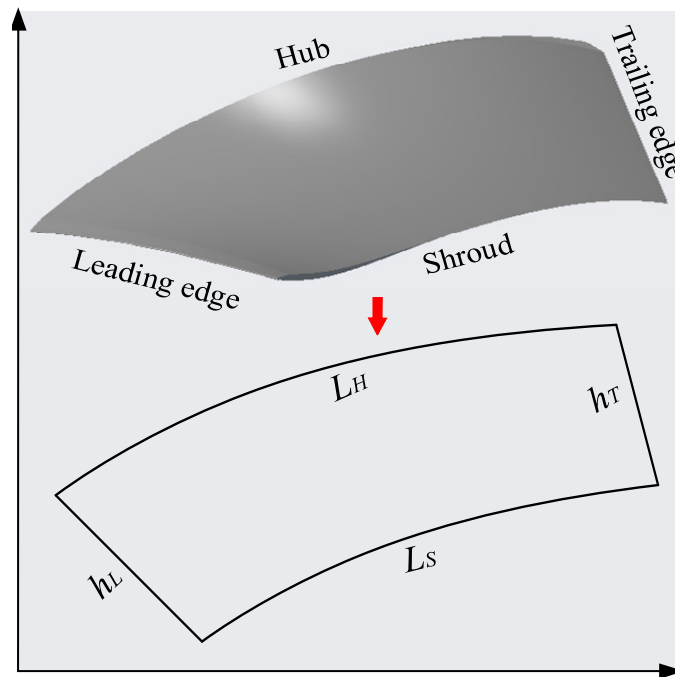


Figure 2. Blade unfolding diagram.

From Formula (1), we can see that the L and h_{imp} are mainly determined by φ , D_1 , D_2 , β_1 , and β_2 . β_1 and β_2 are mainly determined by the velocity triangle of the blade inlet and outlet and are thus kept constant; b_1 is mainly determined by the impeller inlet diameter and has a set value. Therefore, for mixed flow impeller blade types, the L and h_{imp} are mainly controlled by φ and b_2 .

This study utilized an orthogonal test design with 20 different combinations of pack angles ranging from 105° to 125° and outlet widths of 95, 99, 103, and 107. The aim was to investigate how the L and h_{imp} affect the performance of RCPs. The design scheme for the orthogonal tests is provided in Table 2.

Table 2. Impeller designs with different arc lengths and blade heights.

Sample	φ	b_2	L	h_{imp}	L/h_{imp}	$L \times h_{imp}(S)$
1	105	95	244.08	107.5	2.271	26,239
2	110	95	254.67	107.5	2.369	27,377
3	115	95	265.32	107.5	2.468	28,521
4	120	95	276.00	107.5	2.567	29,671
5	125	95	286.73	107.5	2.667	30,824
6	105	99	244.46	109.5	2.232	26,768
7	110	99	255.09	109.5	2.330	27,933
8	115	99	265.79	109.5	2.427	29,104
9	120	99	276.52	109.5	2.525	30,279
10	125	99	287.29	109.5	2.624	31,459
11	105	103	244.86	111.5	2.196	27,302
12	110	103	255.55	111.5	2.292	28,494
13	115	103	266.28	111.5	2.388	29,691
14	120	103	277.06	111.5	2.485	30,893
15	125	103	287.88	111.5	2.582	32,099
16	105	107	245.29	113.5	2.161	27,840
17	110	107	256.03	113.5	2.256	29,059
18	115	107	266.81	113.5	2.351	30,283
19	120	107	277.63	113.5	2.446	31,511
20	125	107	288.50	113.5	2.542	32,745

In this study, entropy production theory is utilized to analyze the distribution of hydraulic losses and the extreme value region of flow losses within the RCP. As the medium being transported is water, it is less affected by temperature changes, so the heat transfer effect can be ignored. Only the specific entropy generation rate $S_{pro,DT}$ caused by the dissipation effect is considered. The internal flow dissipation loss of the RCP is much greater than the wall loss. Therefore, the specific entropy generation rate caused by wall friction is ignored, and the specific entropy generation rate in a turbulent flow $S_{pro,DT}$ is mainly composed of the specific entropy generation rate caused by the time-averaged movement and the fluctuating terms. It can be expressed as

$$S_{pro,DT} = S_{pro,\bar{D}} + S_{pro,D'} \tag{3}$$

The expression for the entropy generation rate caused by the time-averaged movement is

$$S_{pro,\bar{D}} = \frac{\mu}{T} * \left\{ 2 \left[\left(\frac{\partial \bar{u}}{\partial x} \right)^2 + \left(\frac{\partial \bar{v}}{\partial y} \right)^2 + \left(\frac{\partial \bar{w}}{\partial z} \right)^2 \right] + \left(\frac{\partial \bar{u}}{\partial y} + \frac{\partial \bar{v}}{\partial x} \right)^2 + \left(\frac{\partial \bar{u}}{\partial z} + \frac{\partial \bar{w}}{\partial x} \right)^2 + \left(\frac{\partial \bar{v}}{\partial z} + \frac{\partial \bar{w}}{\partial y} \right)^2 \right\} \tag{4}$$

The expression for the entropy generation rate caused by the fluctuation velocity is

$$S_{pro,D'} = \frac{\mu}{T} * \left\{ 2 \left[\left(\frac{\partial u'}{\partial x} \right)^2 + \left(\frac{\partial v'}{\partial y} \right)^2 + \left(\frac{\partial w'}{\partial z} \right)^2 \right] + \left(\frac{\partial u'}{\partial y} + \frac{\partial v'}{\partial x} \right)^2 + \left(\frac{\partial u'}{\partial z} + \frac{\partial w'}{\partial x} \right)^2 + \left(\frac{\partial v'}{\partial z} + \frac{\partial w'}{\partial y} \right)^2 \right\} \tag{5}$$

However, $S_{pro,D'}$ is still an unknown term but may be related to the turbulence model [16]. According to Kock’s entropy production theory [17], the entropy generation rate caused by the fluctuation velocity is defined as

$$S_{pro,D'} = \frac{\rho \varepsilon}{T} \tag{6}$$

The total entropy production of the calculated domain is the volume integral of the dissipation specific entropy generation rate. S_D can be expressed as

$$S_D = \int_V S_{pro,\bar{D}} dV + \int_V S_{pro,D'} dV \tag{7}$$

where μ is the dynamic viscosity; ε is the turbulent dissipation rate; u, v, w are the components of the velocity of the mass in a right-angle coordinate system; and T is the temperature of the fluid mass.

This study utilized the STAR-CCM+ software’s built-in mesh generation module was utilized to generate the mesh. The surface mesh generator model uses the surface remesher and automatic surface repair, whereas the pyramidal mesh generator uses the polyhedral mesh generator. The boundary layer mesh generator selected the prism layer mesher and locally refined the blades of the impeller and guide vane. The mesh of the RCP is displayed in Figure 3. The independence of the fluid calculation domain’s grid for the RCP was examined. Schemes 1 to 5 were established from sparse to dense in proportion of the number of cells for each scheme, as shown in Table 3. When the number of cells reached 1,855,000, the change in RCP efficiency was less than 0.05%. Considering computational resources and the computational accuracy of entropy production, Scheme 3 was selected for numerical simulation.

The fluid medium used in the calculations was water at a temperature of 25 °C. It was assumed to be incompressible with a density of 997.561 kg/m³ and a dynamic viscosity of 8.8871 × 10⁻⁴ Pa·s. The reference pressure was set at 101,325 Pa. The inlet boundary condition was set as a mass flow inlet while the outlet boundary condition was set as a pressure outlet. Interfaces were created for the contact surfaces of each adjacent component and were set as internal interfaces. The realizable $k-\varepsilon$ two-layer turbulence model was utilized as the turbulence model with a computational convergence accuracy of 10⁻⁴.

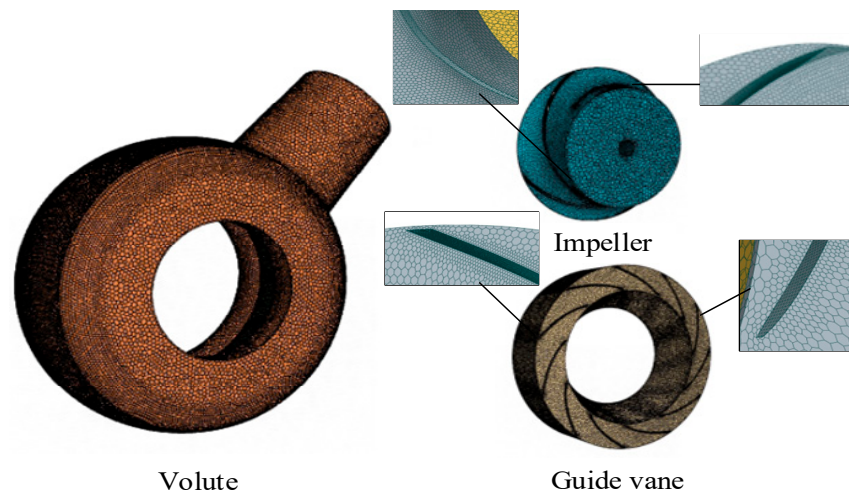


Figure 3. Grid division of the RCP.

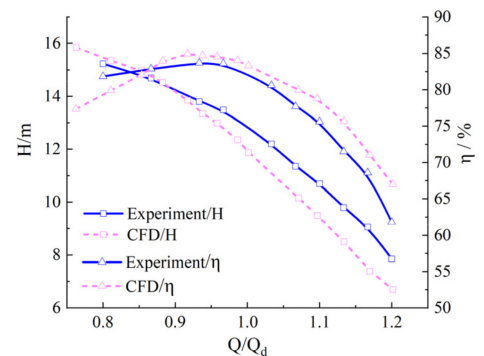
Table 3. Grid independence test.

Scheme	Cell Number	Efficiency/%
Scheme 1	980227	82.1847
Scheme 2	1525249	82.7779
Scheme 3	1855138	82.8299
Scheme 4	2124763	82.8722
Scheme 5	2456409	82.9176

Figure 4a displays the test bench photograph, which includes equipment such as a pressure transmitter, force sensor, torque meter, DN350 electromagnetic flow meter, and pressure sensor. The accuracy of the pressure transmitter is $\pm 0.1\%$, the accuracy of the torque meter is $\pm 0.02\%$, the accuracy of the DN350 electromagnetic flow meter is $\pm 0.5\%$. By using the pump unit comprehensive error, the overall performance of the pump unit system can be evaluated, and the efficiency comprehensive error of the pump unit system can be obtained based on the systematic error and random error of the pump unit system. The accuracy error of the pump unit efficiency in this experiment is $\pm 1.48\%$, which meets the precision requirements of GB33216-89B level and ISO/DIS5198A level, indicating that the experimental results are reliable. Figure 4b shows a comparison between the experiments and simulations. As the simulation and test results exhibit a consistent trend with an error of less than 5%, the simulation data are deemed reliable.



(a) Test bench of model pump



(b) Comparison of experiment and simulation

Figure 4. RCP test bench and comparison curve.

3. Results

The external characteristics of the 20 orthogonal design models are listed in Table 4. It is evident from the table that the efficiency under large flow conditions aligns with the trend of head change, which is primarily influenced by the L and h_{imp} . There is little variation under small flow conditions, while under the design flow condition, the efficiency (E_f) changes slightly but there is a significant change in head. The 5th, 6th, 10th, 11th, 15th, and 16th models exhibit an extensive variation range, with all parameters exhibiting an increasing trend except for the efficiency under the design flow condition. The head also rises when the L is kept constant and the h_{imp} is increased. On the other hand, when the h_{imp} remains unchanged and the L is changed, the head (H) drops. Each group of models maintains a fixed h_{imp} and varies the φ design within the range of 105° to 125° in five-degree increments. Comparing the H of the 1st, 6th, 11th, and 16th models, which have different h_{imp} s but the same L , shows that all have a consistent upward trend, and the efficiency curve also shows a constant upward trend.

Table 4. Table of design characteristics.

Model	0.8Q _d		1.0Q _d		1.2Q _d	
	E _f /%	H/m	E _f /%	H/m	E _f /%	H/m
1	79.198	15.241	81.147	12.878	61.648	8.154
2	81.451	15.286	81.429	12.662	60.102	7.644
3	81.821	15.100	80.838	12.231	57.000	6.939
4	82.153	14.944	78.498	11.575	53.155	6.227
5	83.608	14.795	77.244	11.076	49.688	5.545
6	80.524	15.762	81.650	13.300	67.273	9.184
7	81.151	15.644	81.825	13.090	64.534	8.549
8	81.808	15.202	82.660	12.964	56.892	6.926
9	81.826	15.232	80.759	12.286	56.603	6.955
10	82.097	14.968	78.684	11.680	53.837	6.345
11	79.079	15.697	81.726	13.476	71.571	10.083
12	79.287	15.656	82.173	13.454	68.592	9.381
13	80.602	15.654	81.749	13.144	67.113	8.915
14	81.440	15.523	82.566	12.935	65.172	8.366
15	81.773	15.252	81.246	12.427	57.658	7.109
16	78.169	15.770	82.052	13.973	74.934	10.898
17	78.612	15.691	82.516	13.745	71.814	10.157
18	79.807	15.661	82.637	13.521	70.355	9.660
19	80.689	15.638	83.132	13.407	69.443	9.256

A correlation analysis was conducted to investigate the relationship between the geometric parameters of the impeller, including L , h_{imp} , L/h_{imp} and S , with efficiency and head performance. Figure 5 indicates that S has a weak correlation with efficiency and head performance, while L and h_{imp} have a strong correlation with efficiency and head performance. Under both 1.0Q_d and 1.2Q_d conditions, the impact of each factor on head and efficiency is similar. Specifically, L , L/h_{imp} and S are all negatively correlated with head and efficiency, whereas h_{imp} is positively correlated with head and efficiency. Moreover, the contribution of each geometric parameter to head and efficiency can be ranked as follows: $L/h_{imp} > h_{imp} > L > S$.

Under the 0.8Q_d condition, each factor has opposite effects on efficiency and head performance. Specifically, L , L/h_{imp} , and S positively affect efficiency, while the head is negatively correlated with them. The contribution of each geometric parameter to efficiency can be ranked as follows: $L/h_{imp} > L > h_{imp} > S$; and for head performance, the order is $L/h_{imp} > h_{imp} > L > S$. Based on the correlation analysis, it can be concluded that smaller L/h_{imp} and higher h_{imp} lead to higher efficiency and head performance under design flow and large flow conditions. However, larger L/h_{imp} and lower h_{imp} under small flow conditions result in higher efficiency and lower head performance.

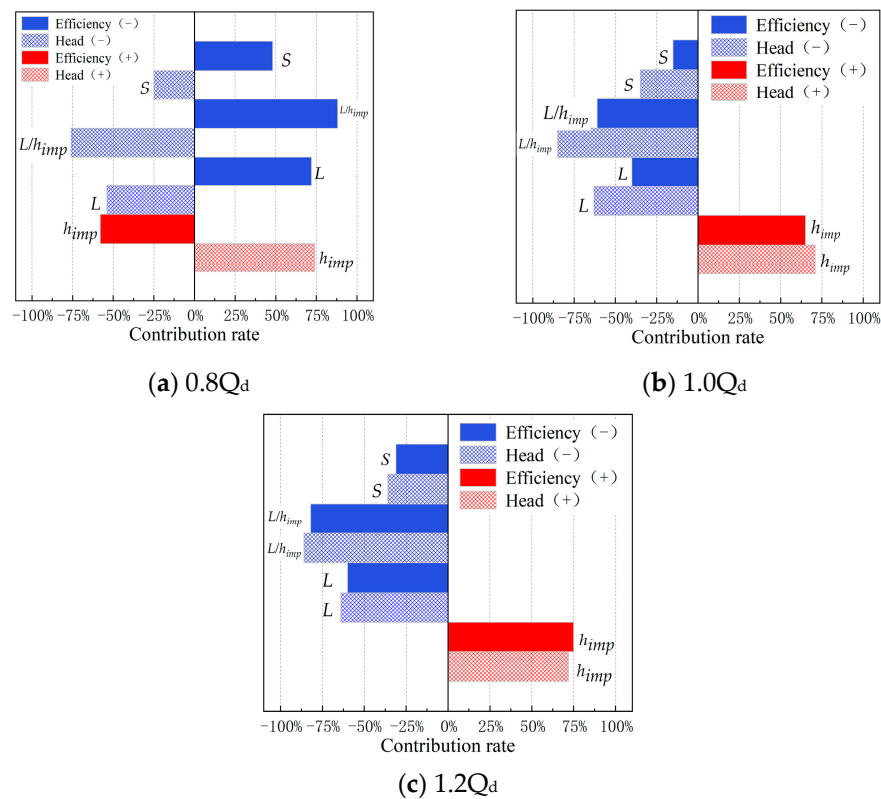


Figure 5. Influence of different geometric parameters on the hydraulic characteristics.

The head and efficiency indicators of twenty impeller models were comprehensively analyzed under different flow conditions, and four impeller models with different L/h_{imp} , L , and h_{imp} were selected to analyze these parameters' effects on the RCP's work and influx energy conversion mechanism. The selected models were Model 6, 8, 16, and 18, as shown in Figure 6, and named Model I, II, III, and IV, respectively. By comparing these models, analyzing constant h_{imp} , increasing L , and larger L/h_{imp} , it was found that the efficiency increased at both small flow conditions and design flow conditions, while the efficiency at large flow conditions tended to decrease significantly. When the L remained unchanged, and the h_{imp} decreased, the efficiency increased under small flow conditions but decreased under design flow conditions and large flow conditions.

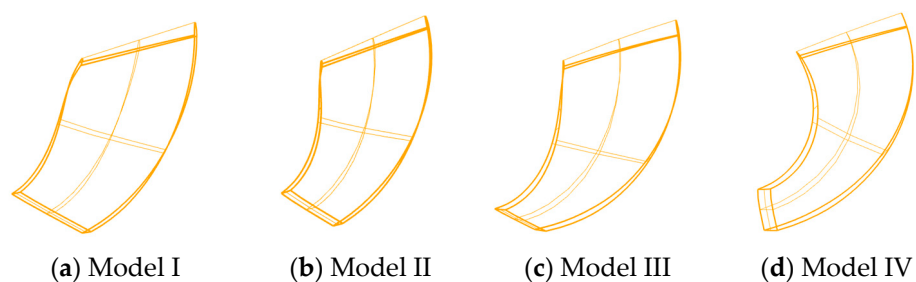


Figure 6. Characteristics of the four model impeller blade shapes.

4. Discussion

Figure 7 presents the axial velocity streamline of the RCP under different conditions. A significant number of low-velocity vortex groups can be observed inside the spherical volute, mainly distributed downstream of the volute (A) and the inner part of the diffusion segment (B). Under small flow conditions, the flow in the pump casing is more uniform, with fewer vortex groups and higher flow velocities in the impeller and guide vane flow paths. Models I and III have shorter L and larger velocity gradients within the impeller,

resulting in significantly larger high-speed vortex groups that have a significant impact on the inlet side of the guide vane. The fluid outflow after the flow state of the guide vane is worse, and it has a more significant impact on the inner wall of the volute, forming a pronounced secondary flow and vortex groups in the volute.

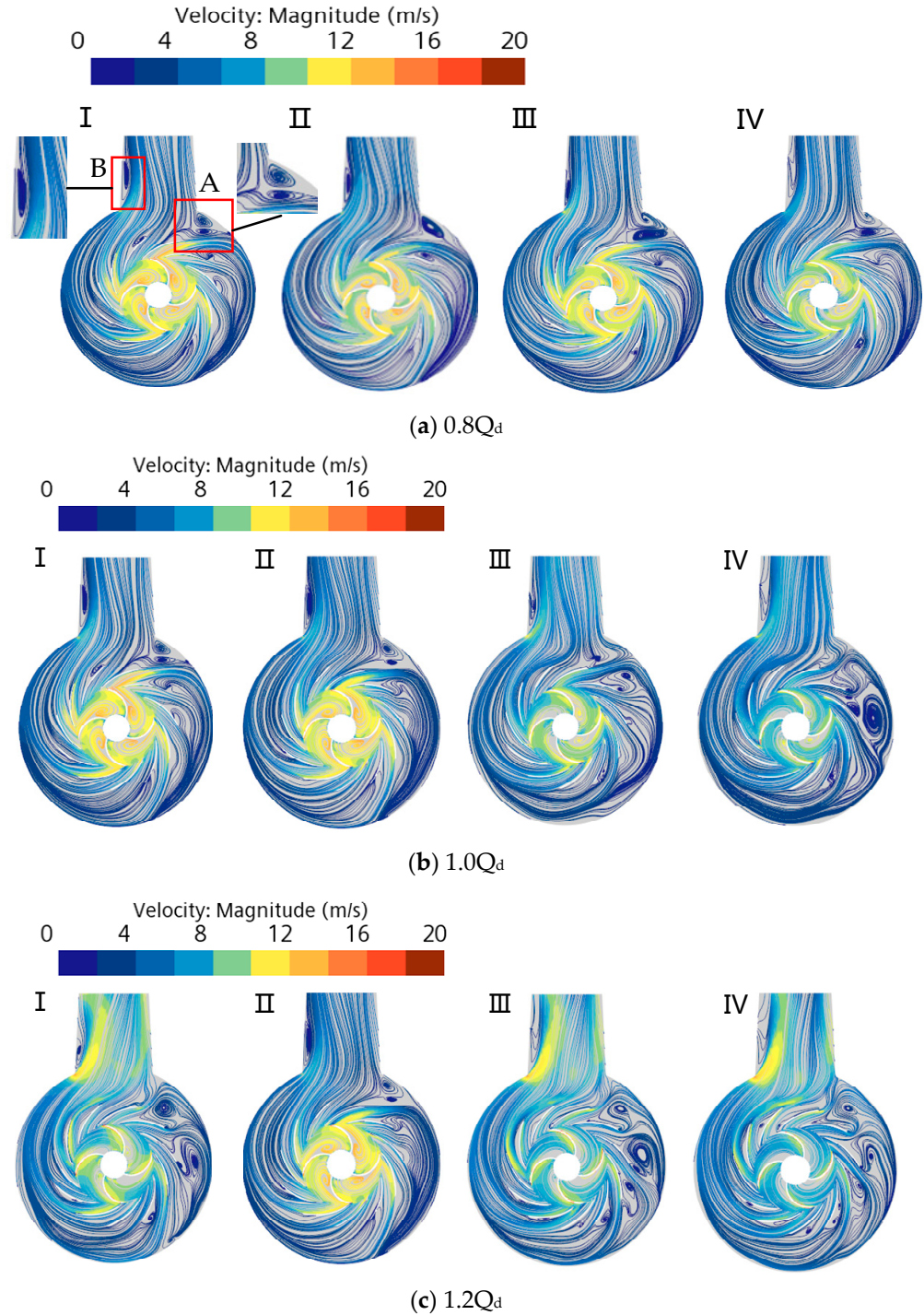


Figure 7. Axial velocity flowline of RCP under different flow conditions.

Model IV impeller exhibits significantly smaller vortex groups at high velocities in the impeller flow path with more uniform velocity gradient changes. As a result, the fluid follows a better streamline after entering the guide vane and volute, leading to smaller vortex groups in the A and B zones. Therefore, under small flow conditions, the impeller is slender (with a large L/h_{imp}), and it can perform more adequate work.

Under the $1.0Q_d$ condition, the Model I and II impellers exhibit obvious high-velocity vortex groups, and there is a high-velocity zone and boundary layer separation in the guide vane. However, the flow in the volute is significantly better, with an obvious low-velocity vortex zone in the B zone. The flow in the Model IV impeller is the best, but there is a large vortex in the volute, and there is backflow phenomenon at the guide vane outlet. At $1.2Q_d$, models I, III, and IV all have good flow patterns within the impeller, but there is reflux at the exit of the guide vane channel, a large number of vortex groups in the volute, and an obvious high-speed jet in the B zone. Model II has an obvious vortex group in the impeller, with high velocity backflow in the guide vane channel, but it performs relatively better inside the volute. At $0.8Q_d$ and $1.0Q_d$ conditions, Model IV has the best flow pattern with uniform velocity gradient changes within the impeller, resulting in the highest efficiency. However, at $1.2Q_d$ conditions, Model IV has a large number of vortex groups inside the volute, leading to the lowest efficiency.

Based on the above analysis, it is evident that the L , h_{imp} , and L/h_{imp} of the impeller have a significant impact on the flow inside the RCP. A detailed analysis of dissipation losses within the impeller, guide vane, and volute flow channel of the RCP is necessary to assess the impeller's influence on the flow inside the RCP and to gain a more comprehensive understanding of the work and energy conversion mechanism of the RCP impeller.

Figures 8 and 9 illustrate the entropy production distribution on the impeller's working surface and suction surface. As depicted in Figure 8, hydraulic losses on the blade's working surface are primarily concentrated at the blade outlet and outer edge of the blade. As the flow rate increases, the fluid's impact on the blade intensifies, leading to boundary layer separation and the generation of wake flow.

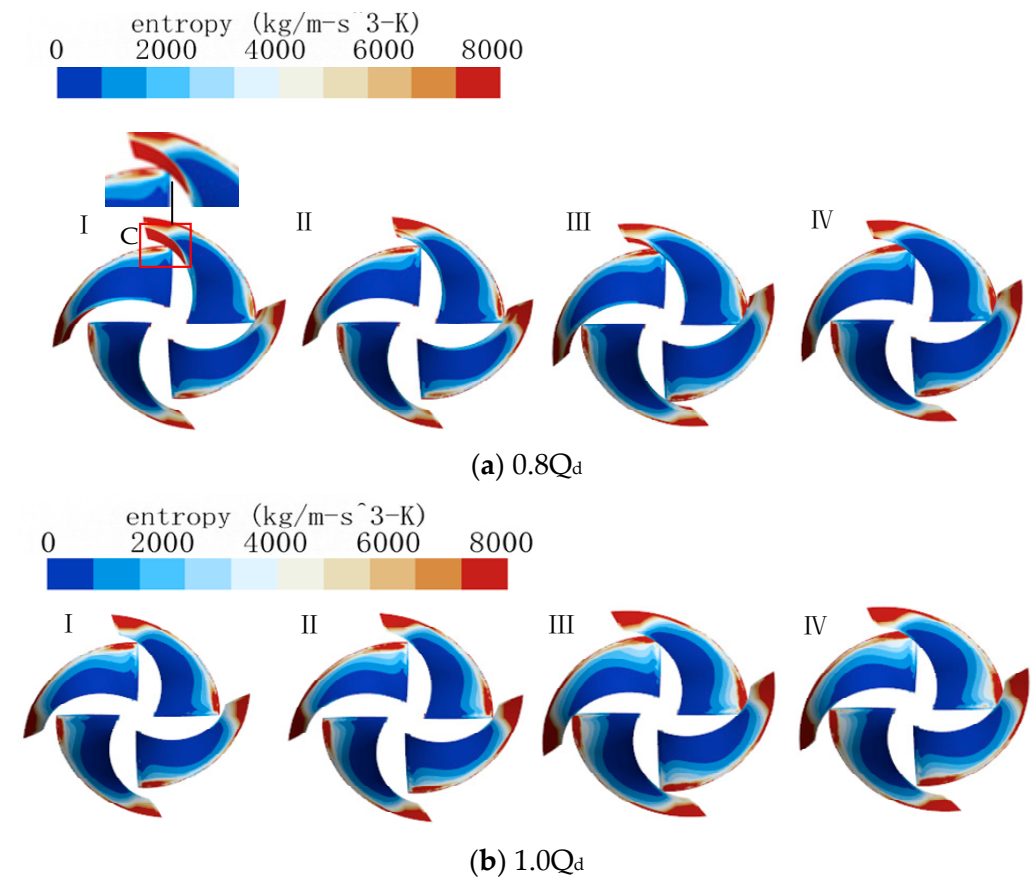


Figure 8. Cont.

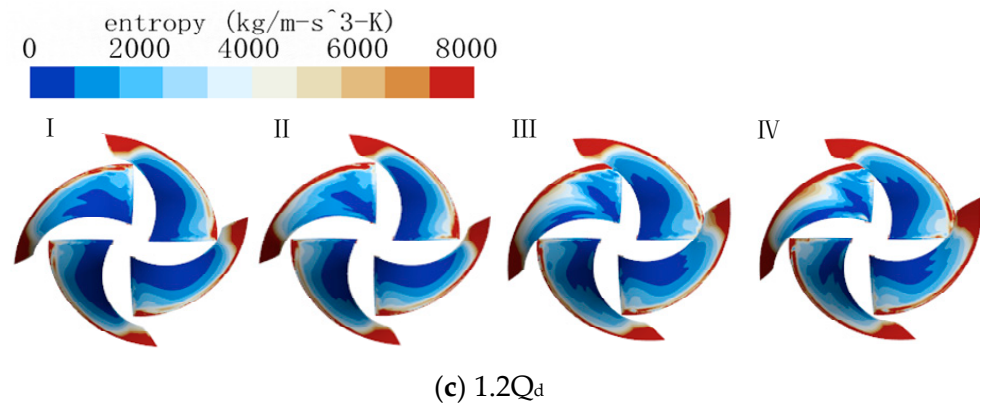


Figure 8. Entropy production distribution on impeller blade working surface.

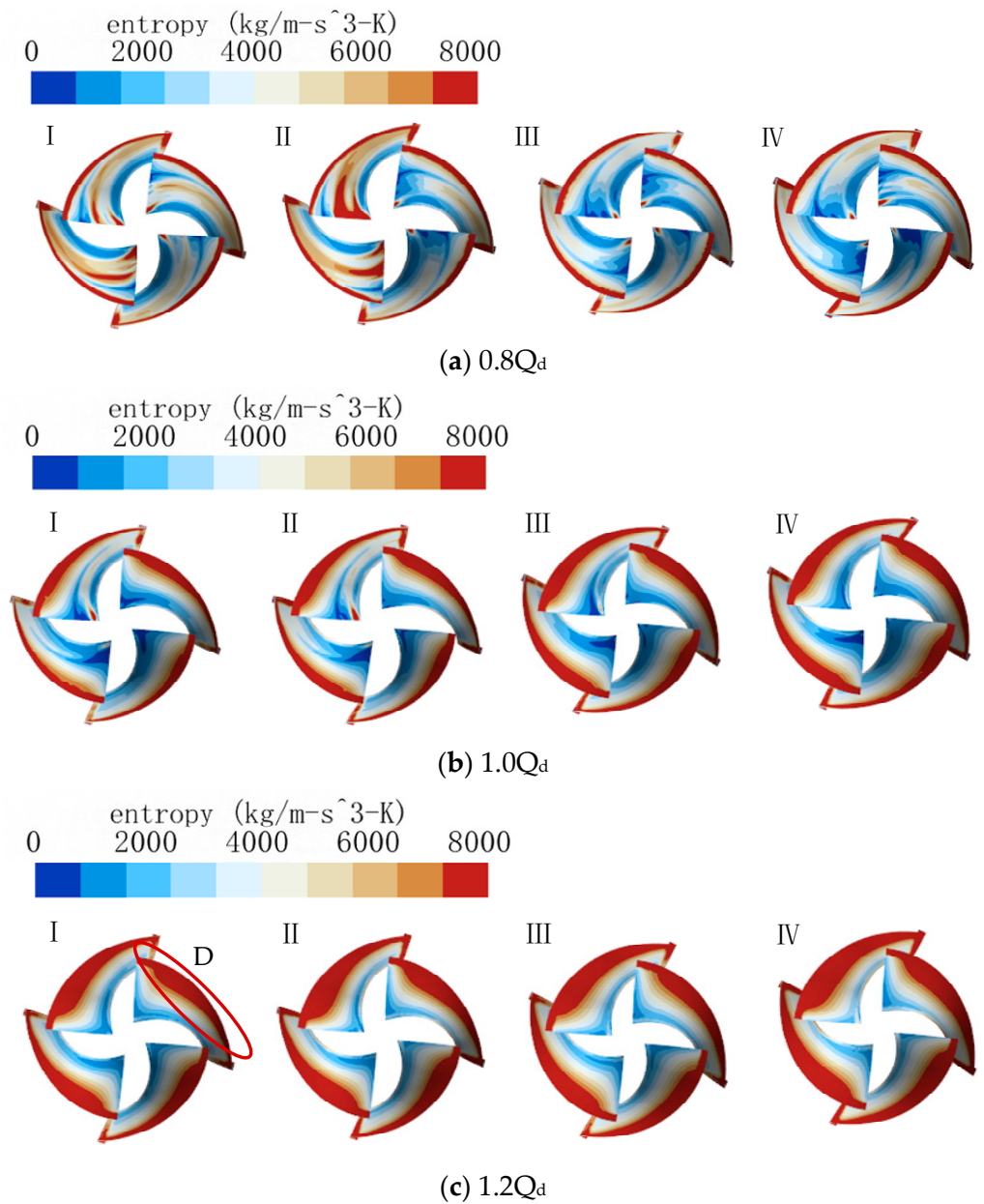


Figure 9. Entropy production distribution on impeller blade suction surface.

Consequently, there is an increase in hydraulic losses at the blade outlet and outer edge. Figure 8a shows that at small flow conditions, the entropy production on the working surfaces of different impellers is concentrated near the blade outlet, specifically in the area close to the front cover. Moreover, the entropy production distribution on the suction surface is significantly greater than on the working surface. Model I and III blades have higher entropy production on the outlet edge's inner (C) side due to fluid decoupling. In contrast, models II and IV exhibit less loss in the C zone and higher loss at the outlet close to the rear cover. As the L increases and the h_{imp} decreases, the flow channel narrows, causing the blades to be more constrained to the fluid.

Comparing Figures 8 and 9, the hydraulic losses on the impeller mainly occur on the suction side of the impeller. Upon examination of Figure 9's entropy distribution diagram for the impeller's suction surface, it becomes apparent that hydraulic losses at the outer edge of the blade (D) increase as the flow rate increases. Moreover, when the L increases, hydraulic losses in the D zone increase due to hydraulic impact and friction losses. As the L remains unchanged but the h_{imp} increases, the hydraulic loss at the inlet of the impeller's suction side decreases. Model II, with its smaller L and h_{imp} , has a greater blade curvature, resulting in a larger hydraulic loss at the inlet. At small flow conditions, secondary flow occurs at the blade inlet, creating a sizable area of hydraulic loss at the inlet due to the narrow flow path of Model II. At large flow conditions, the range of hydraulic losses in the D zone expands due to the rapid impingement and friction of the fluid.

Figure 10 displays the entropy distribution of the axial section of the RCP, providing a visual representation of the internal hydraulic losses in the RCP. The area of the entropy generation rate distribution reflects the efficiency of the RCP, with larger areas indicating higher losses and lower efficiency. Figure 10 shows that hydraulic losses within the RCP are mainly located at the impeller outlet, guide vanes, inner flow channel and E zone.

At $0.8Q_d$ flow condition, the energy losses are mostly concentrated in the guide vane channel. At $1.2Q_d$ flow condition, the energy losses concentrate at the E zone. Under $1.0Q_d$ condition, the overall loss is small, but the loss in the guide vane channel of Model II is larger. Based on the aforementioned velocity flow field analysis, fluid is likely to experience turbulence when flowing along the guide vane channel, which can cause phenomena such as impact. These effects can lead to higher pressure areas in the local guide vane region.

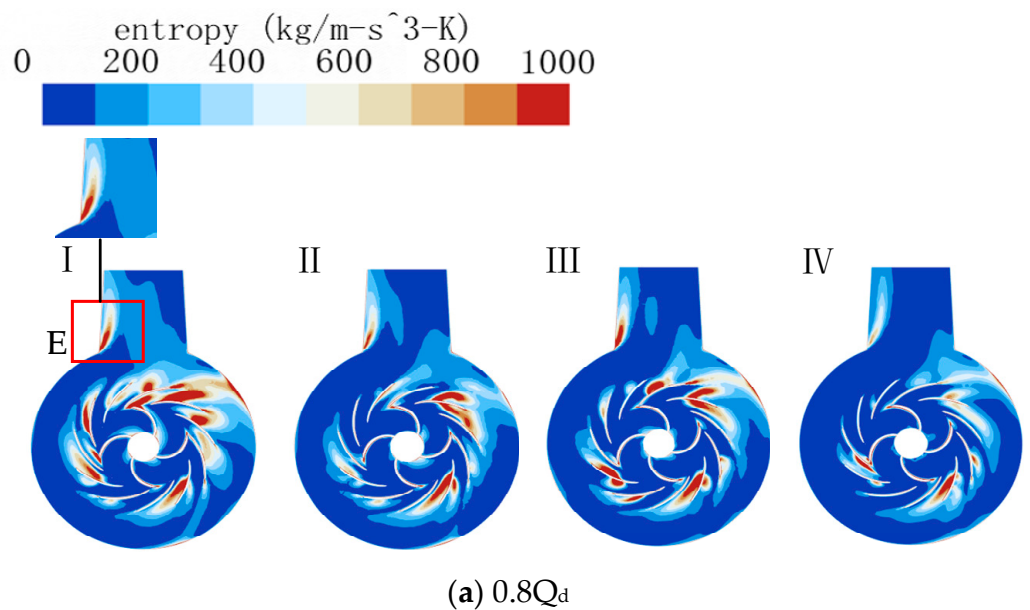


Figure 10. Cont.

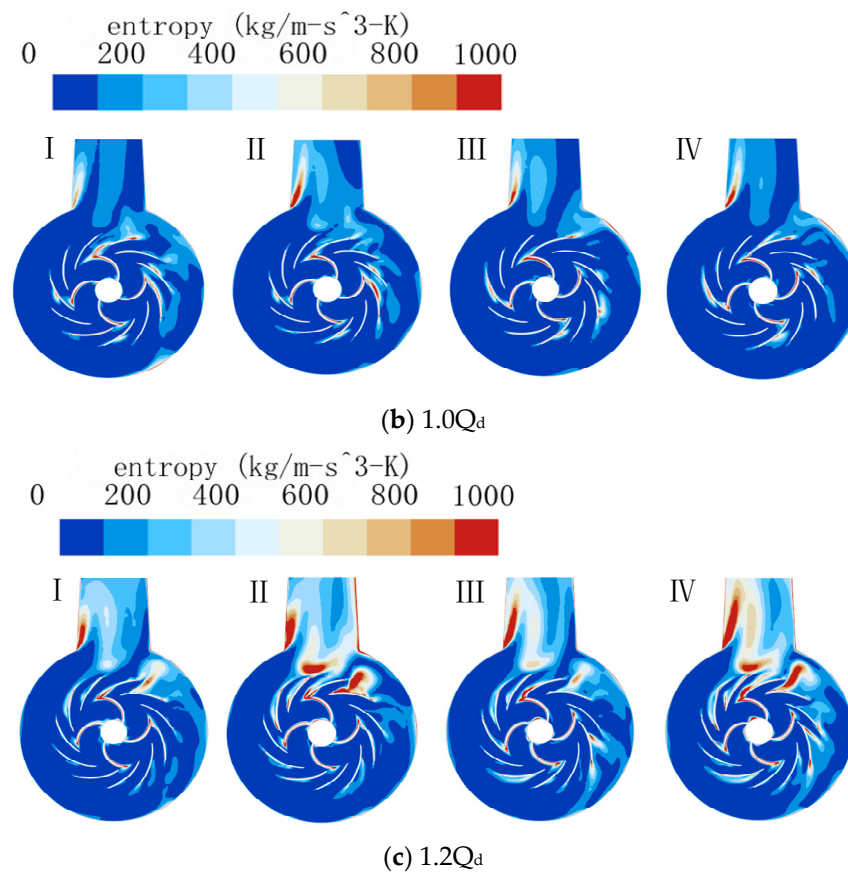


Figure 10. Entropy production distribution of RCP under three flow rates.

For models I, II, III, and IV, the loss in the E zone increases with increasing L or decreasing h_{imp} . Model I has smaller losses in the E zone, but greater losses at the impeller outlet and the inlet of the guide vane. Model IV has the smallest entropy distribution area while Model I has the largest entropy distribution area under small flow conditions.

Due to the increased flow velocity at the impeller outlet of Model I, rotor-stator interaction occurs, resulting in larger losses at both the guide vane outlet and within the guide vane’s flow channel. To address this issue, increasing the arc length can result in more uniform flow in the pump, lower flow velocity at the impeller outlet, and reduced losses. By increasing the L , the flow in the pump becomes more uniform, flow velocity at the impeller outlet decreases and losses are reduced. When the L is unchanged and the h_{imp} is reduced, the flow velocity in the impeller channel decreases. This reduces the influence of static and dynamic blade interference, reducing guide vane channel losses. The highest efficiency occurs at an arc height ratio of 2.427, while the lowest efficiency occurs at an arc height ratio of 2.161.

Under large flow conditions, models II and IV experience greater losses due to their smaller impeller h_{imp} . When the fluid flows out of the guide vane and into the outlet section, mutual extrusion can occur, resulting in chaotic flow and causing higher losses. Additionally, losses increase at the corner where the volute connects to the exit section as the L/h_{imp} increases. Model I, with L/h_{imp} of 2.161, is the most efficient, while Model IV, with L/h_{imp} of 2.427, is the least efficient.

To further investigate the internal flow losses of the RCP under various flow conditions, the percentage of losses in each component of the RCP and the entropy production of each component was analyzed. Figures 11 and 12 show that the flow loss in the volute is the primary contributor, and as the flow rate increases, the loss in the volute also increases. At 1.2 Q_d condition, the entropy production in the volute accounts for as much as 76%.

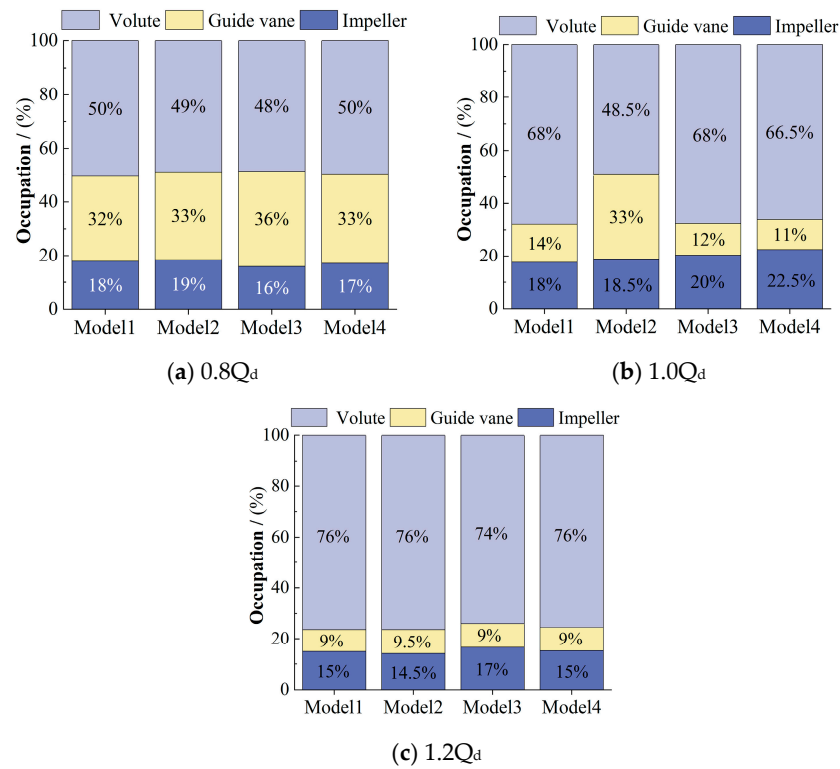


Figure 11. Entropy production ratio of each component of the RCP under the three flow rates.

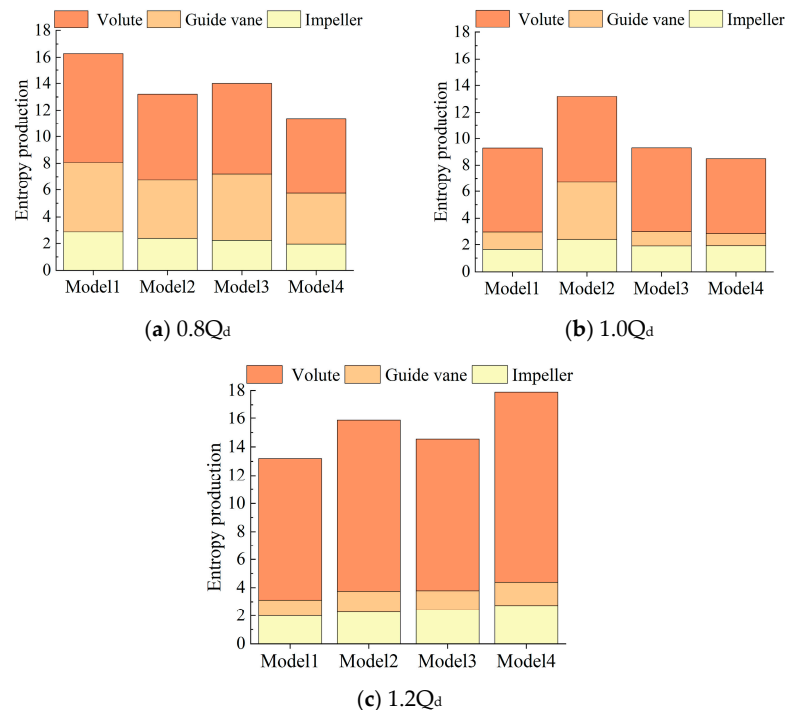


Figure 12. Entropy production of each component of the RCP under the three flow rates.

When the flow rate changes from 0.8Q_d to 1.0Q_d, the proportion of entropy production of Model I and II impellers remains unchanged, while the proportion of entropy production of Model III and IV impellers increases. Although the proportion of Model I and II remains unchanged according to Figure 12, the entropy generation rate of Model I impeller decreases, while that of the Model II impeller increases. This indicates that Model I is suitable for

operation under $1.0Q_d$ conditions, while Model II, with its reduced h_{imp} and narrower flow channel, is suitable for operation under low flow conditions.

The guide vane entropy production of Model I, III, and IV decreases greatly, indicating that the impeller and guide vane coupling is better. The fluid entering the guide vane can better fit the linear flow of the guide vane. On the other hand, the guide vane entropy production of Model II increases because the short and narrow impeller blade shape leads to a higher velocity of fluid entering the guide vane, causing impact losses to the guide vane.

As the flow rate expands from $1.0Q_d$ to $1.2Q_d$, the impeller entropy generation rate decreases, and the actual entropy production value also decreases. The entropy production of the guide vane is smaller under large flow conditions. Still, the entropy production of Model II drops significantly due to turbulent flow occurring in the volute which increases losses.

5. Conclusions

The CFD method combined with entropy production theory was used to analyze the effects of variations in L , h_{imp} , and L/h_{imp} on the hydraulic performance of the model under different conditions of the RCP. Based on the analysis, the following conclusions were drawn:

1. The different impeller types have a significant impact on the hydraulic performance of the RCP. The impeller blade with L/h_{imp} of 2.427 exhibits the highest efficiency at $0.8Q_d$ and $1.0Q_d$ conditions, while the impeller blade with L/h_{imp} of 2.161 has the highest efficiency at the $1.2Q_d$ condition. Conversely, the impeller blade with L/h_{imp} of 2.427 has the lowest efficiency at the $1.2Q_d$ condition. These findings suggest that selecting the appropriate impeller design is critical for optimizing the hydraulic performance of RCPs under different conditions.
2. Increasing the L of the impeller leads to a smoother blade profile and reduces the occurrence of secondary flow phenomena. Additionally, under low flow conditions, increasing the L while decreasing the h_{imp} narrows the flow channel, allowing the fluid to better utilize the blade shape to do work. This optimization can lead to improved hydraulic performance and efficiency of the RCP.
3. The dissipation loss of the different models varies greatly as the flow rate increases. When the flow rate changes from $0.8Q_d$ to $1.0Q_d$, the entropy production of the guide vane decreases significantly for Models I, III, and IV, while the entropy production of the guide vane for Model II increases. Under large flow conditions, the entropy production of the guide vane for each model is lower, and the entropy production of the guide vane for Model II decreases significantly. However, the loss in the volute increases, indicating that Model II is better suited for operation at low flow conditions. These results highlight the importance of selecting the appropriate model based on the conditions to optimize the hydraulic performance of the RCP.

Author Contributions: Conceptualization, Q.F. and Y.L.; methodology, W.Z.; software, Y.Z.; validation, R.Z. and Q.F.; formal analysis, Y.Z.; data curation, W.Z.; writing—original draft preparation, Y.Z.; writing—review and editing, Y.Z.; visualization, Q.F.; supervision, R.Z.; project administration, R.Z.; funding acquisition, Q.F. All authors have read and agreed to the published version of the manuscript.

Funding: Joint Funds of the National Natural Science Foundation of China (U20A20292); National Key Research and Development Program of China (2018YFB0606105); Natural Science Foundation of Jiangsu Province (BK20210771); National Natural Science Foundation of China (51906085); China Postdoctoral Science Foundation Funded Project (2021M701847 and 2022M711768).

Institutional Review Board Statement: Not applicable.

Informed Consent Statement: Not applicable.

Data Availability Statement: Not applicable.

Conflicts of Interest: The authors declare no conflict of interest.

References

1. Zhong, Y.; Liu, Y.; Zhou, W.; Xia, D. Investigation on methodology of coastdown analysis and design for reactor coolant pump. *Nucl. Power Eng.* **2017**, *38*, 84–88.
2. Cai, L.; Zhang, L. Brief introduction of a pressurized water reactor main pump in a nuclear power plant. *Water Pump Technol.* **2007**, *176*, 1–5+9.
3. Yang, M.; Lu, S.; Gao, B. Influence of blade thickness on energy performance of mixed flow nuclear main pump. *Fluid Mach.* **2015**, *43*, 28–32.
4. Yang, M.; Zhang, Y.; Zhou, Z.; Wang, Z.; Gao, B. Influence of different blade trailing edges on energy performance of impellers in a mixed-flow nuclear main pump. *J. Harbin Eng. Univ.* **2017**, *38*, 230–234.
5. Qiu, W.; Zhu, R.; Wang, X. Influence of optimization of impeller geometric parameters on coast-down performance of nuclear reactor coolant pump. *J. Drain. Irrig. Mach. Eng.* **2019**, *37*, 1019–1024.
6. Srivastava, S.; Roy, A.K.; Kumar, K. Design of a mixed flow pump impeller blade and its validation using stress analysis. *Procedia Mater. Sci.* **2014**, *6*, 417–424. [[CrossRef](#)]
7. Xie, R.; Hao, M.; Jin, W.; Wang, X.; Cheng, Z.; Lu, Z. Hydraulic Model Design and Optimization of Nuclear Reactor Coolant Pump Based on Approximation Model. *J. Eng. Thermophys.* **2016**, *37*, 1427–1431.
8. Lu, Y.; Wang, X.; Liu, H.; Li, Y. Investigation of the effects of the impeller blades and vane blades on the CAP1400 nuclear coolant pump's performances with a united optimal design technology. *Prog. Nucl. Energy* **2020**, *126*, 103426. [[CrossRef](#)]
9. Lu, Y.M.; Wang, X.F.; Wang, W.; Zhou, F.M. Application of the modified inverse design method in the optimization of the runner blade of a mixed-flow pump. *Chin. J. Mech. Eng.* **2018**, *31*, 105. [[CrossRef](#)]
10. Wang, X.; Lu, Y.; Zhu, R.; Fu, Q.; Yu, H.; Chen, Y. Study on bidirectional fluid-solid coupling characteristics of reactor coolant pump under steady-state condition. *Nucl. Eng. Technol.* **2019**, *51*, 1842–1852. [[CrossRef](#)]
11. Ye, D.X.; Lai, X.D.; Zhang, X.; Wang, Q.L. Hydraulic optimization of impeller blade in reactor coolant pump base on Kriging model. *IOP Conf. Ser. Earth Environ. Sci.* **2019**, *240*, 032051. [[CrossRef](#)]
12. Wang, H.; Long, B.; Wang, C.; Han, C.; Li, L. Effects of the impeller blade with a slot structure on the centrifugal pump performance. *Energies* **2020**, *13*, 1628. [[CrossRef](#)]
13. Al-Obaidi, A.R. Investigation of the influence of various numbers of impeller blades on internal flow field analysis and the pressure pulsation of an axial pump based on transient flow behavior. *Heat Transf.* **2020**, *49*, 2000–2024. [[CrossRef](#)]
14. Al-Obaidi, A.R. Analysis of the effect of various impeller blade angles on characteristic of the axial pump with pressure fluctuations based on time-and frequency-domain investigations. *Iran. J. Sci. Technol. Trans. Mech. Eng.* **2021**, *45*, 441–459. [[CrossRef](#)]
15. Li, H.; Chen, Y.; Yang, Y.; Wang, S.; Bai, L.; Zhou, L. CFD simulation of centrifugal pump with different impeller blade trailing edges. *J. Mar. Sci. Eng.* **2023**, *11*, 402. [[CrossRef](#)]
16. Zhou, L.; Hang, J.; Bai, L.; Krzemianowski, Z.; El-Emam, M.A.; Yasser, E.; Agarwal, R. Application of entropy production theory for energy losses and other investigation in pumps and turbines: A review. *Appl. Energy* **2022**, *318*, 119211. [[CrossRef](#)]
17. Kock, F.; Herwig, H. Entropy production calculation for turbulent shear flows and their implementation in CFD codes. *Int. J. Heat Fluid Flow* **2005**, *26*, 672–680. [[CrossRef](#)]

Disclaimer/Publisher's Note: The statements, opinions and data contained in all publications are solely those of the individual author(s) and contributor(s) and not of MDPI and/or the editor(s). MDPI and/or the editor(s) disclaim responsibility for any injury to people or property resulting from any ideas, methods, instructions or products referred to in the content.